Lu *et al. Energy Mater* 2024;4:400038
DOI: 10.20517/energymater.2023.117

Energy Materials

Supplementary Materials

Modulating the graphitic domains of hard carbons via tuning resin crosslinking degree to achieve high rate and stable sodium storage

Zhixiu Lu, Xiuping Yin, Yelin Ji, Caixia Li, Ruixiao Wang, Shenqi Li, Tao Yuan, Yufeng Zhao*

College of Sciences & Institute for Sustainable Energy, Shanghai University, Shanghai 200444, China.

***Correspondence to:** Prof. Yufeng Zhao, College of Sciences & Institute for Sustainable Energy, Shanghai University, No. 99 Shangda Road, Baoshan District, Shanghai 200444, China. E-mail: yufengzhao@shu.edu.cn

We report a hard carbon (HC) material derived from 3-aminophenol formaldehyde resin (AFR) with better rate performance, higher initial coulombic efficiency (ICE) and capacity via adjusting the crosslinking degree of the AFR precursor. We discover that a resin precursor with a higher crosslinking degree tends to produce HC with higher carbon yield, a larger d_{002}, fewer defects, and a lower surface area.

Supplementary Table 1. Physical parameters for 0.46-AFR-HC, 0.90-AFR-HC and 1.80-AFR-HC

		0.46-AFR-HC	0.90-AFR-HC	1.80-AFR-HC
	d_{002} (nm)	0.388	0.384	0.372
TEM	L_c (nm)	1.40	1.36	1.32
	L_a (nm)	2.64	2.59	2.56
	d_{002} (nm)	0.401	0.389	0.374
XRD	L_c (nm)	1.46	1.42	1.33
	L_a (nm)	3.01	2.89	2.88

$d_{002} = n\lambda/2\sin\theta = 0.154187/2\sin\theta$, $L = K\gamma/B\cos\theta$, $N = Lc/d_{002}+1$, $\boldsymbol{K}$ is the Scherrer constant (usually set as 0.98), $\boldsymbol{\gamma}$ is the wavelength of the X-ray beam, $\boldsymbol{B}$ is the full width at half maximum (FWHM) value of the (002) and (100) peak, $\boldsymbol{2\theta}$ is the diffraction angle, and $\boldsymbol{L}$ is the average thickness in the per-pendicular direction of the crystal plane. $\boldsymbol{L_a}$: the apparent layer-plane length parallel to the fiber axis; $\boldsymbol{L_c}$: the apparent crystallite thickness; $\boldsymbol{d_{002}}$: the average interlayer distance[1-3].

Supplementary Table 2. Raman parameters for 0.46-AFR-HC, 0.90-AFR-HC and 1.80-AFR-HC

		A_D	A_G	A_D/A_G
	0.46-AFR-HC	85.43817	60.85909	1.4039
	0.90-AFR-HC	95.1652	58.9377	1.6146
	1.80-AFR-HC	104.3127	60.7502	1.7171
Raman		I_D	I_G	I_D/I_G
	0.46-AFR-HC	0.9491	0.9968	0.9521
	0.90-AFR-HC	0.9723	0.9815	0.9906
	1.80-AFR-HC	0.9974	0.956	1.0433

Supplementary Table 3. Pore structure and specific surface area information for 0.46-AFR-HC, 0.9-AFR-HC and 1.80-AFR-HC

N_2	BET surface area (m^2/g)	CO_2	Micropore surface area (m^2/g)
0.46-AFR-HC	11.1750	0.46-AFR-HC	506.4595
0.90-AFR-HC	35.7286	0.90-AFR-HC	518.7026
1.80-AFR-HC	52.8906	1.80-AFR-HC	634.4605

Supplementary Table 4. Atomic ratios of elements C, N, and O in 0.46-AFR-HC, 0.90-AFR-HC and 1.80-AFR-HC from XPS

	C (at%)	N (at%)	O (at%)
0.46-AFR-HC	93.29	1.27	5.36
0.90-AFR-HC	92.63	1.28	5.98
1.80-AFR-HC	92.07	1.44	6.4

Supplementary Table 5. The compaction density of 0.46-AFR-HC, 0.90-AFR-HC and 1.80-AFR-HC

	Compaction density (g/cm^3)
0.46-AFR-HC	0.82
0.90-AFR-HC	0.79
1.80-AFR-HC	0.75

Supplementary Table 6. Summary of representative publications with high capacity of HC and other anode materials previously reported in the literature

Materials	Capacity ($mAh \cdot g^{-1}$)	Rate capability ($mAh \cdot g^{-1}$)	Temperature (℃)	Ref.
Seedpod-HC	328	85 @ 1 $A \cdot g^{-1}$	1,200	[4]
Pitch-C	250	124 @ 10 $A \cdot g^{-1}$	1,000	[5]
O-carbon	380	152 @ 2 $A \cdot g^{-1}$	1,600	[6]
N-HC	364	214 @ 10 $A \cdot g^{-1}$	1,200	[7]
HC	320	80 @ 5 C	1,200	[8]
Pitch and resin-HC	350	141 @ 20 $A \cdot g^{-1}$	1,000	[9]
Cu-carbon microcuboid	201	136 @ 2 $A \cdot g^{-1}$	600	[10]
0.46-AFR-HC	383	140 $mAh \cdot g^{-1}$ @ 20 $A \cdot g^{-1}$	1,300	This work

Supplementary Table 7. Summary of representative publications with high ICE of HC previously reported in the literature

Materials	ICE (%)	Electrolyte	Ref.
HCNS	82	1 M $NaPF_6$ in diglyme	[7]
HC-1	79	1 M $NaPF_6$ in TEGDME	[8]
Pitch and resin-HC	63	1 M $NaPF_6$ in diglyme	[9]
Cu-carbon microcuboid	60	1 M $NaCF_3SO_3$ in diglyme	[10]
HC-2	75	1 M $NaPF_6$ in diglyme	[2]
0.46-AFR-HC	82	1 M $NaPF_6$ in diglyme	This work

Supplementary Table 8. EIS fitting data for 0.46-AFR-HC, 0.90-AFR-HC and 1.80-AFR-HC electrodes

Samples	Cycles	R_s	R_{SEI}	R_{ct}
0.46-AFR-HC	10	10.3	2.6	3.6
0.90-AFR-HC	10	10.4	3.9	7.9
1.80-AFR-HC	10	10.4	7.3	11.8

R_s: Internal resistance including the resistances of the electrolyte solution and electrodes; R_{SEI}: interfacial resistance of electrode due to formation of SEI; R_{ct}: resistance associated with charge transfer.

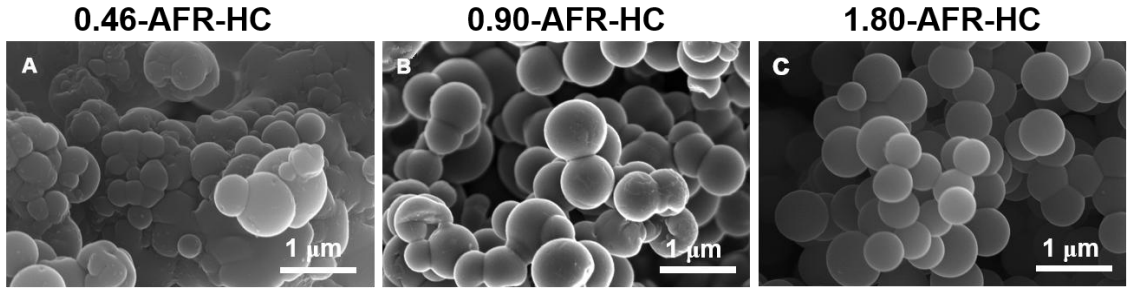

Supplementary Figure 1. SEM images for (A) 0.46-AFR-HC; (B) 0.90-AFR-HC; and (C) 1.80-AFR-HC.

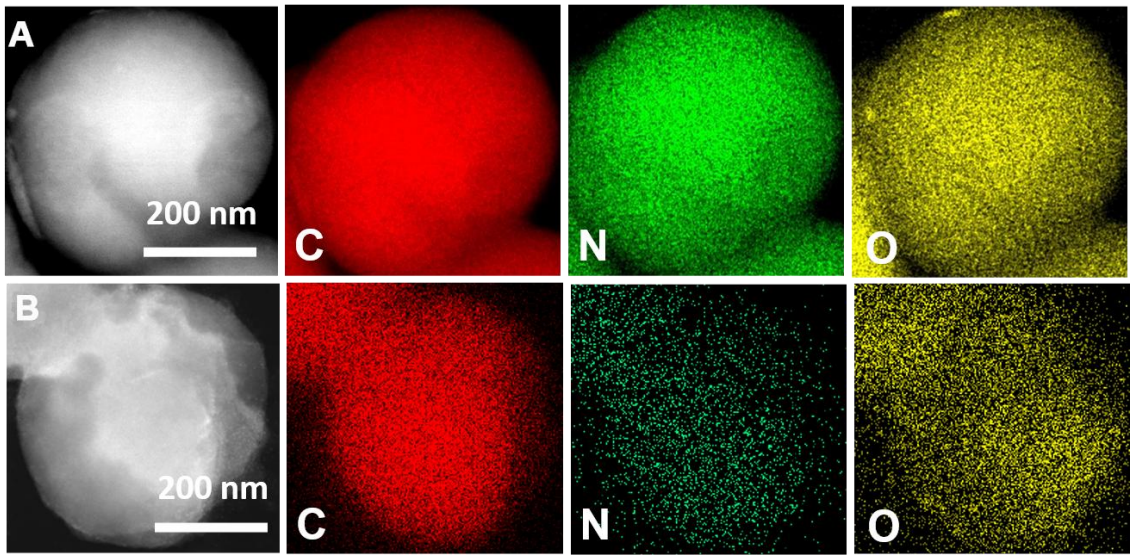

Supplementary Figure 2. Energy-dispersive X-ray spectroscopy mapping images for (A) 0.46-AFR-HC and (B) 1.80-AFR-HC.

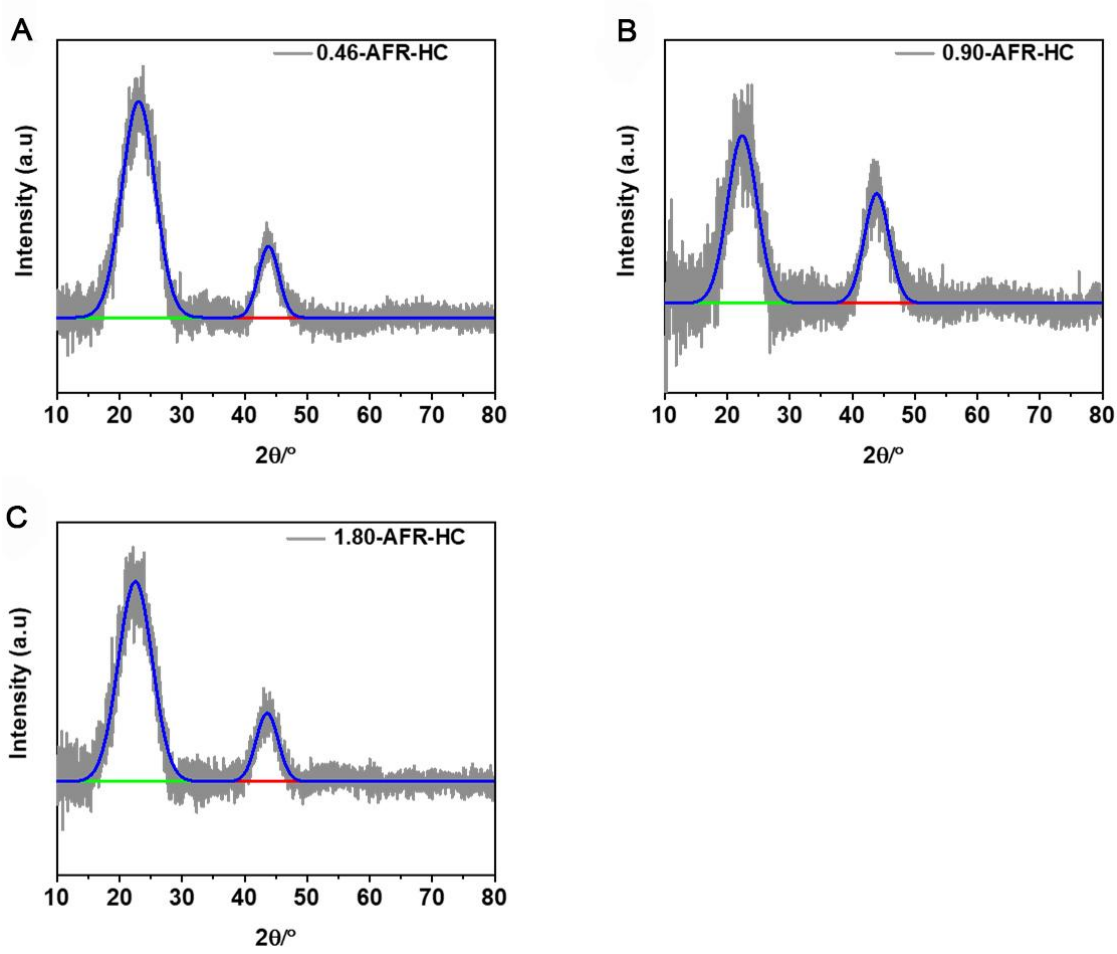

Supplementary Figure 3. XRD patterns. (A) 0.46-AFR-HC; (B) 0.90-AFR-HC; and (C) 1.80-AFR-HC.

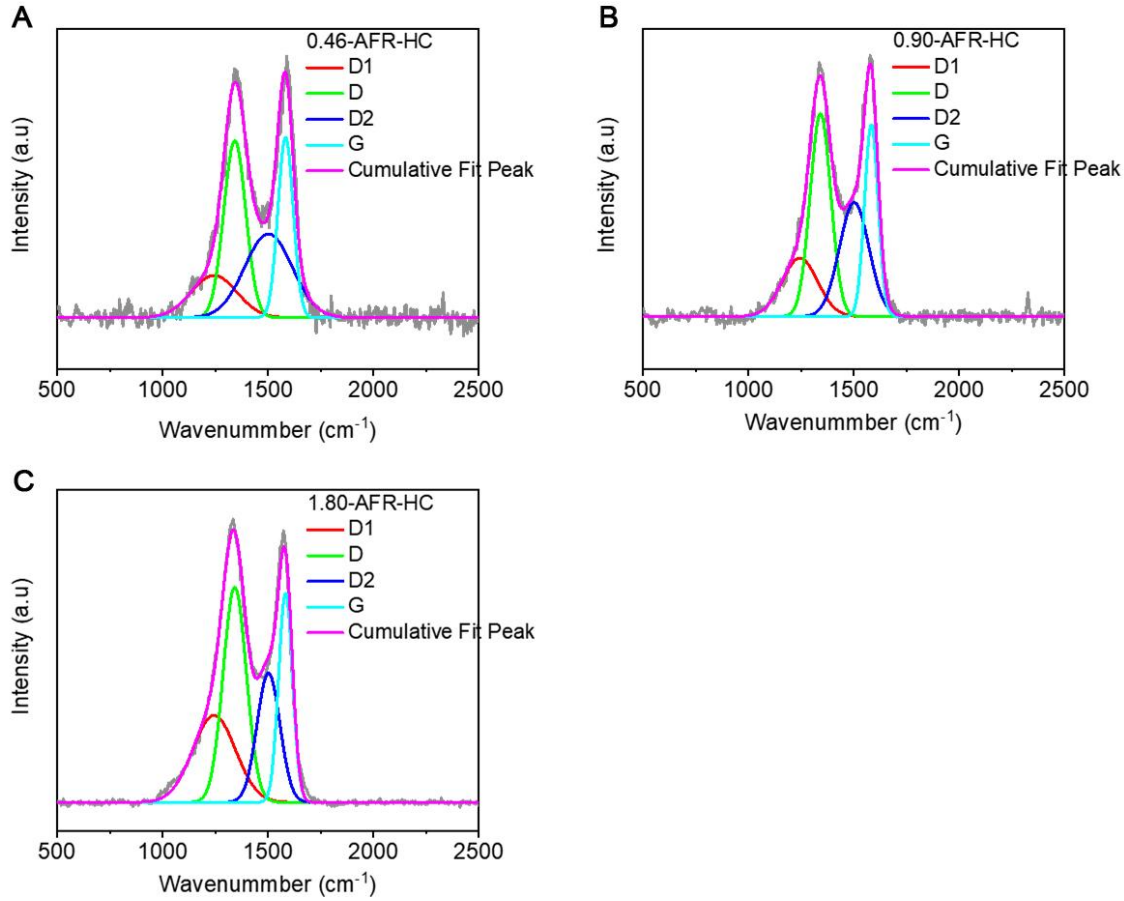

Supplementary Figure 4. Fitted Raman spectra. (A) 0.46-AFR-HC; (B) 0.90-AFR-HC; and (C) 1.80-AFR-HC.

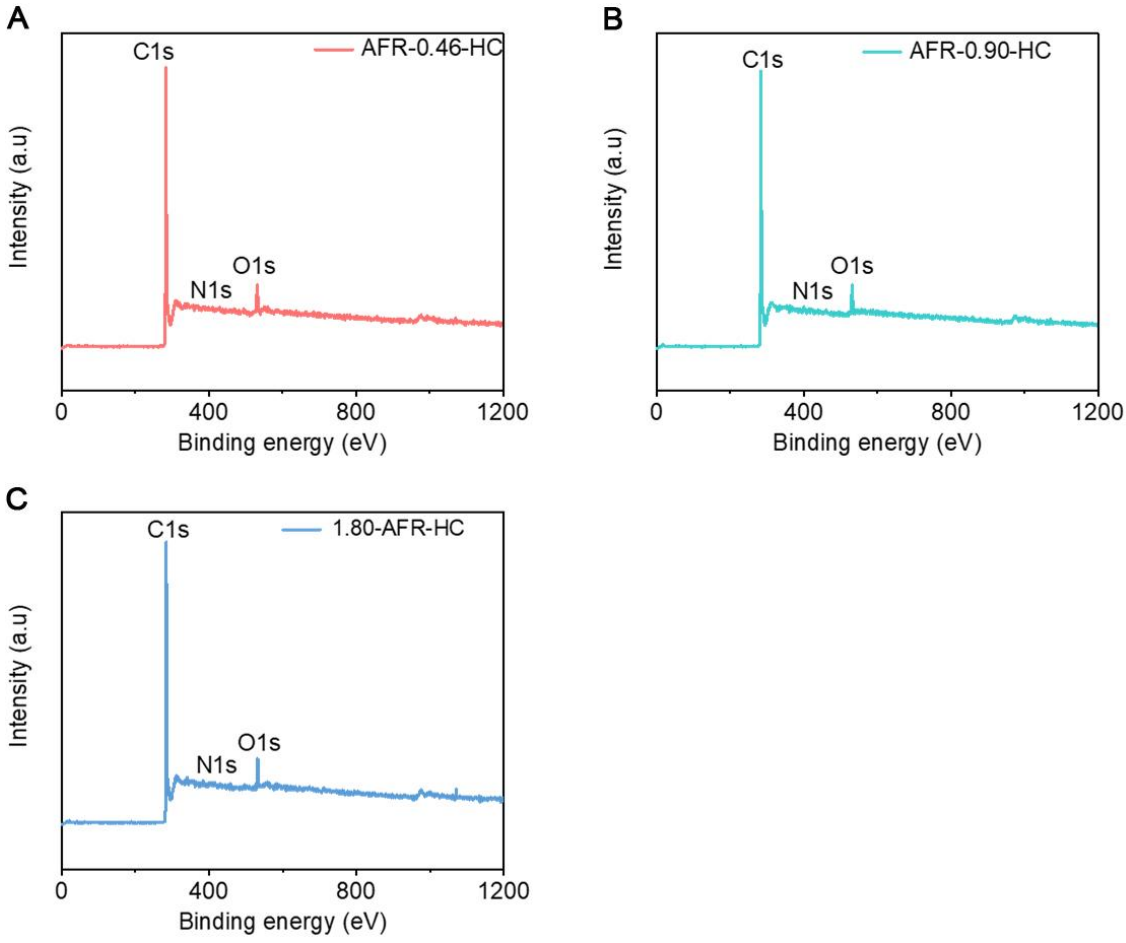

Supplementary Figure 5. The full XPS spectra. (A) 0.46-AFR-HC; (B) 0.90-AFR-HC; (C) 1.80-AFR-HC.

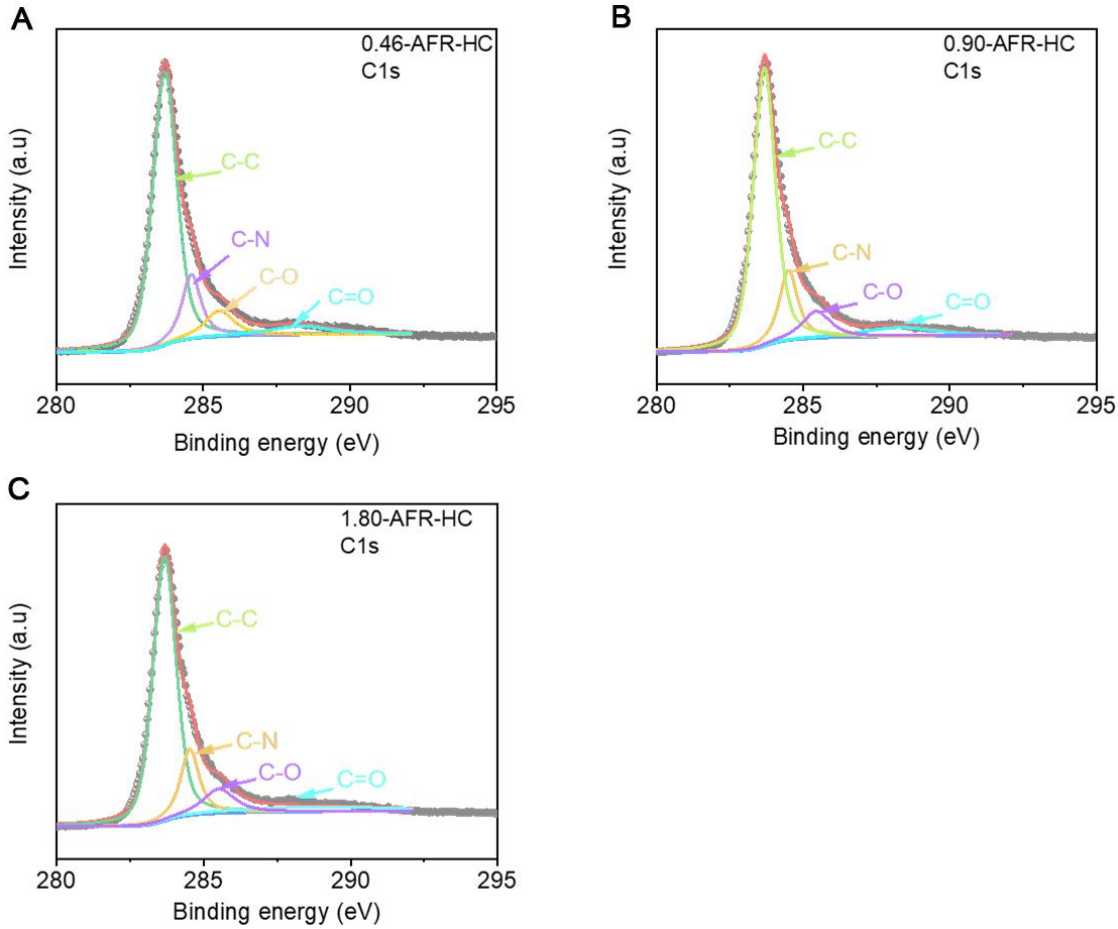

Supplementary Figure 6. The high-resolution XPS of C 1s spectra. (A) 0.46-AFR-HC; (B) 0.90-AFR-HC; (C) 1.80-AFR-HC.

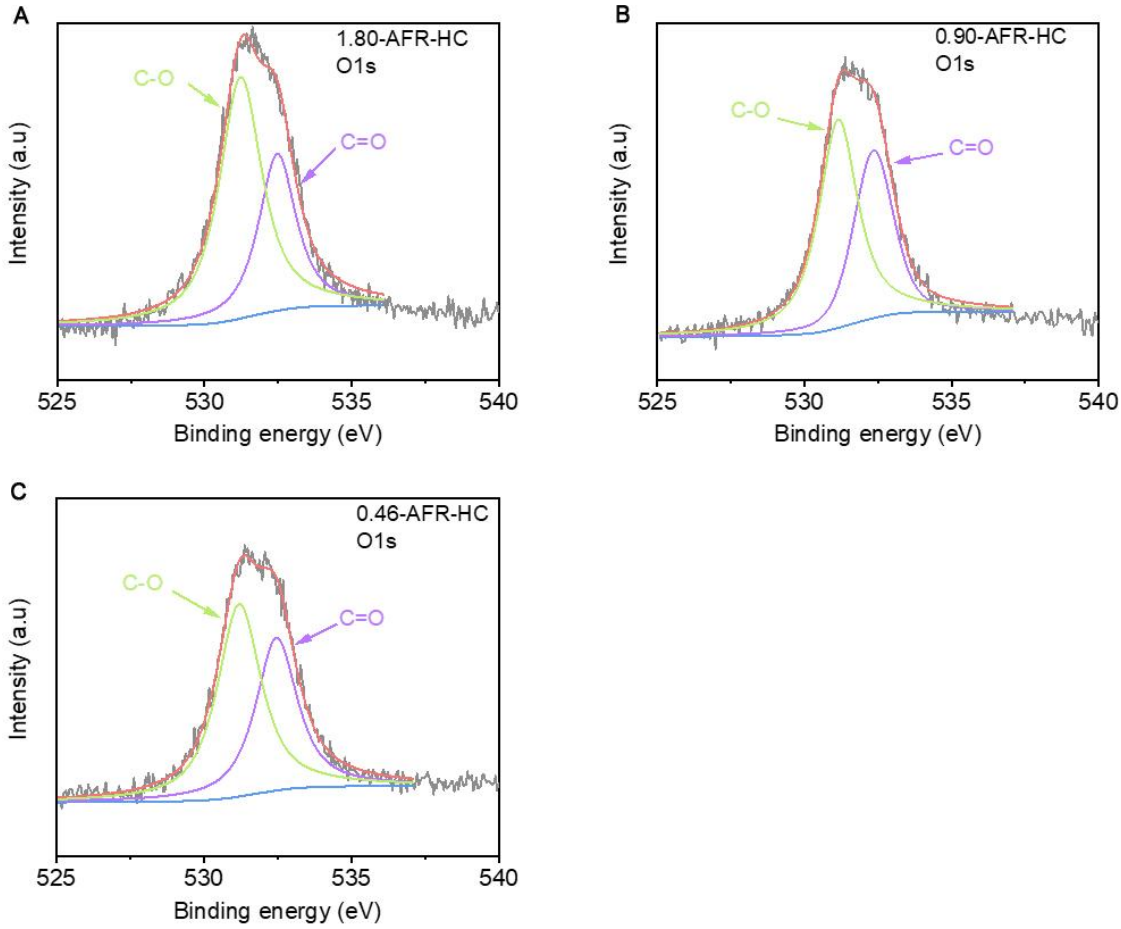

Supplementary Figure 7. The high-resolution XPS of O 1s spectra. (A) 1.80-AFR-HC; (B) 0.90-AFR-HC; (C) 0.46-AFR-HC.

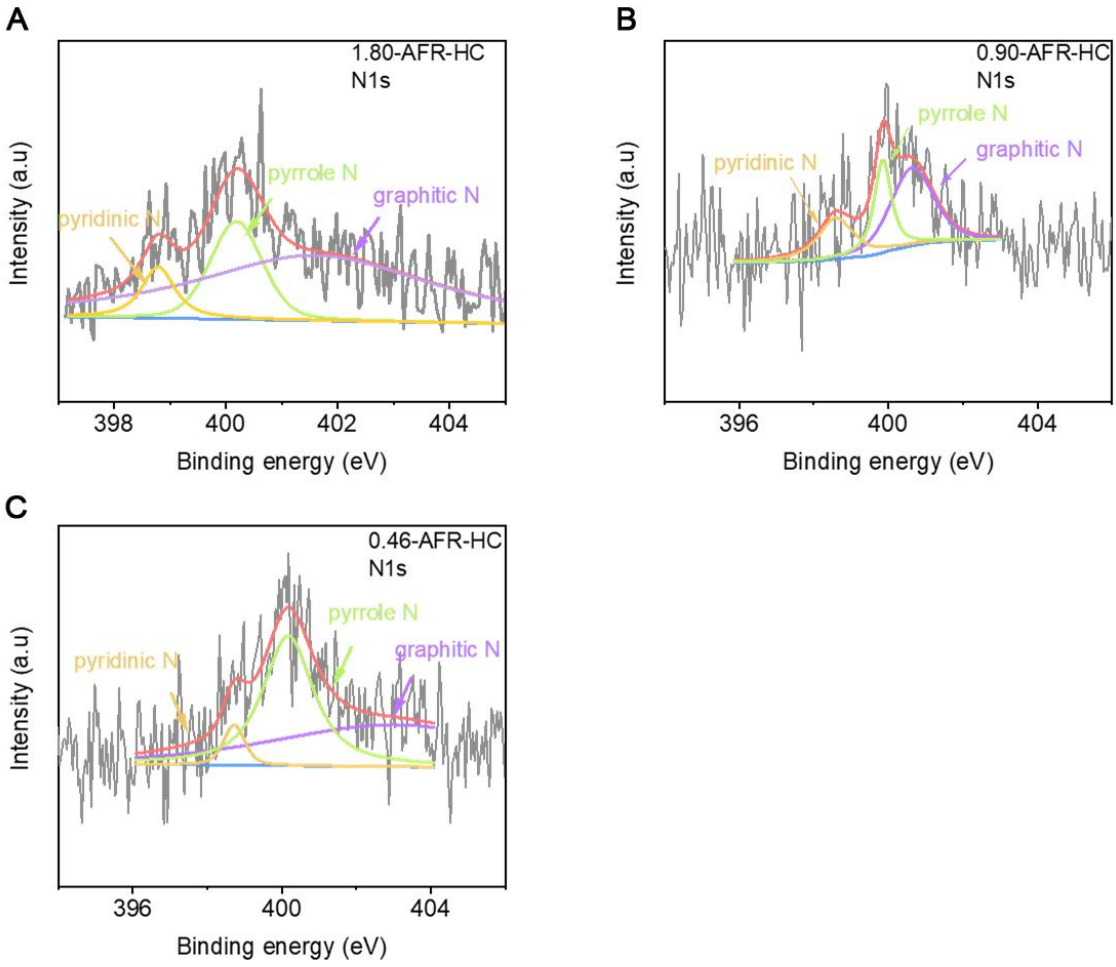

Supplementary Figure 8. The high-resolution XPS of N 1s spectra. (A) 1.80-AFR-HC; (B) 0.90-AFR-HC; (C) 0.46-AFR-HC.

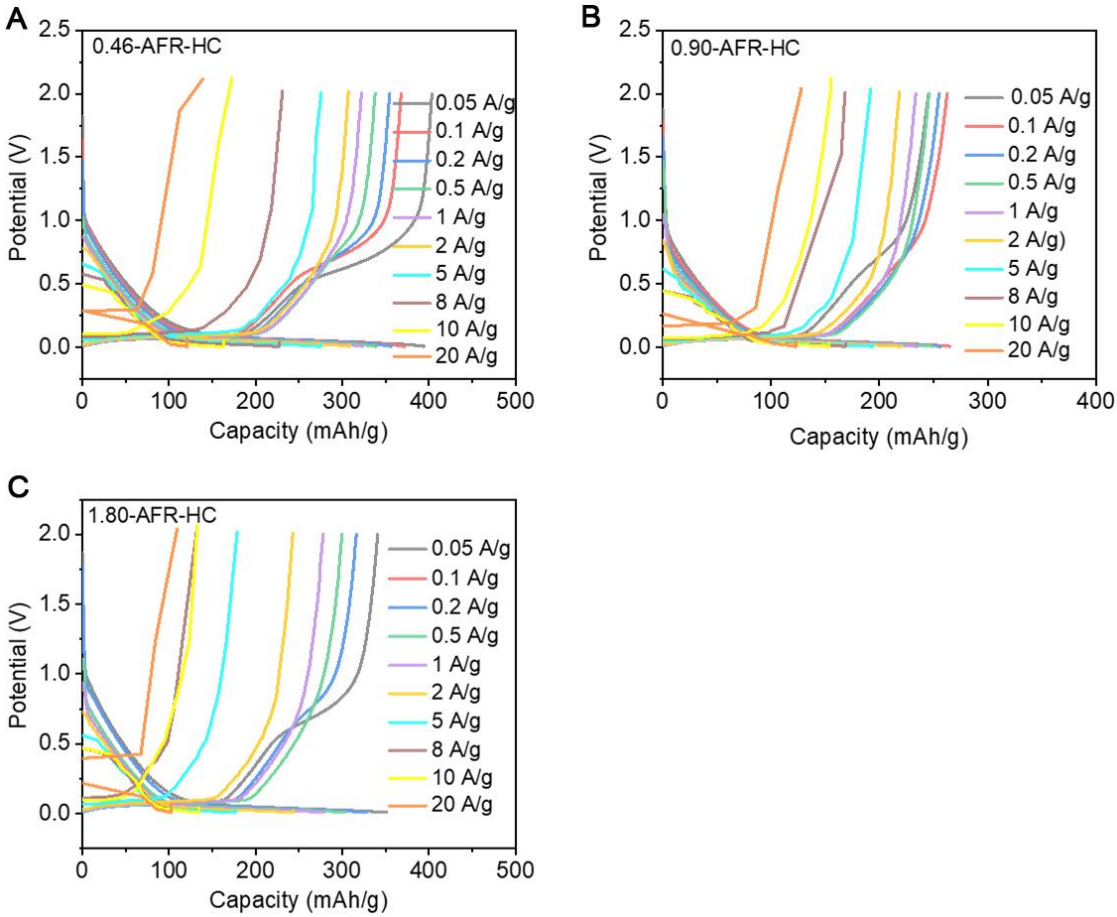

Supplementary Figure 9. The discharge-charge curves at different current densities (A) 0.46-AFR-HC; (B) 0.90-AFR-HC; (C) 1.80-AFR-HC.

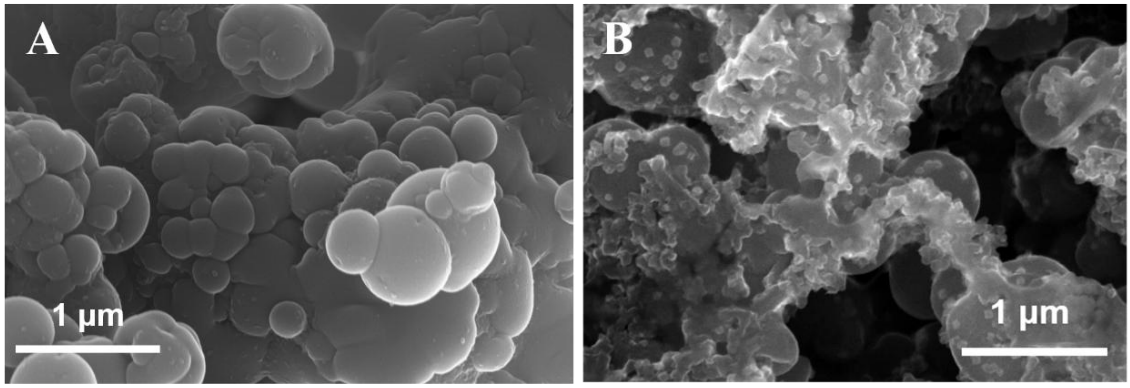

Supplementary Figure 10. (A) SEM images of 0.46-AFR-HC electrodes; (B) SEM images of 0.46-AFR-HC electrodes (0.1 $A \cdot g^{-1}$, 1,000th cycle, 25 ℃).

As shown in Supplementary Figure 10, the morphology of 0.46-AFR-HC can be maintained even after 1,000 cycles, demonstrating the good structural stability of 0.46-AFR-HC. Further HR-TEM images [Supplementary Figure 11] show that a 7-nm-thickness SEI layer is formed on the surface of 0.46-AFR-HC after 50 cycles, which is more uniform and thinner than that of 0.90-AFR-HC (12 nm) and 1.80-AFR-HC (15 nm). The uniform and thin SEI enable the faster interfacial Na^+ transportation, thus leading to higher ICE and rate capability.

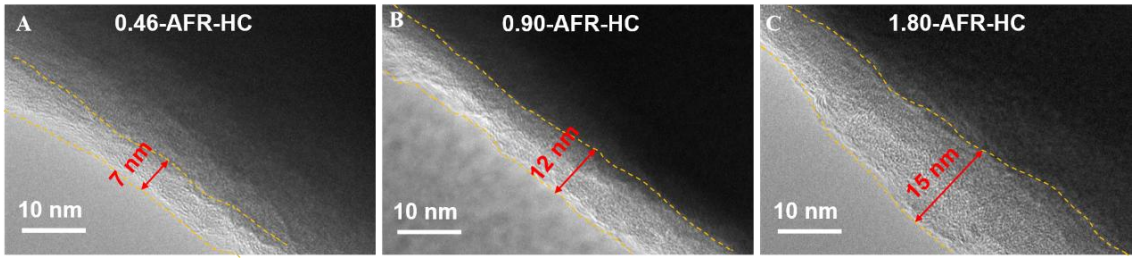

Supplementary Figure 11. HRTEM images of (A)0.46-AFR-HC; (B) 0.90-AFR-HC; and (C) 1.80-AFR-HC electrodes (0.1 $A \cdot g^{-1}$, 50th cycle, 25 ℃).

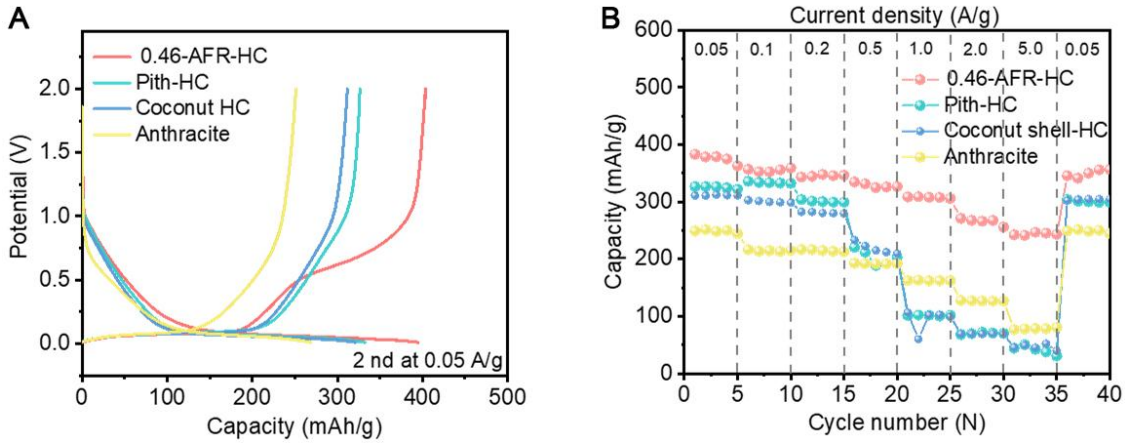

Supplementary Figure 12. (A) The GCD curves (the second cycle) of different hard carbons; (B) Rate performance of different types hard carbons.

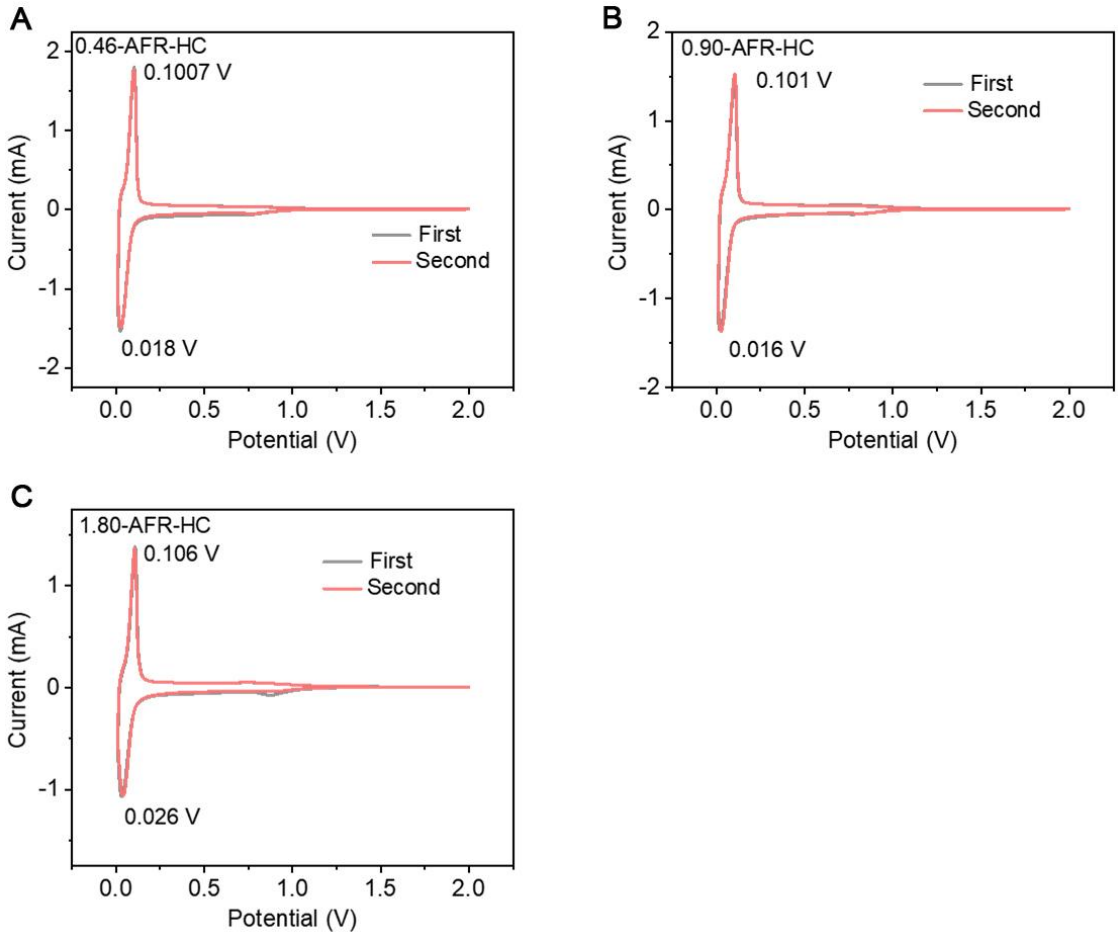

Supplementary Figure 13. Cyclic voltammetry curves at scan rates of 0.2 $mV \cdot s^{-1}$. (A) 0.46-AFR-HC; (B) 0.90-AFR-HC; (C) 1.80-AFR-HC.

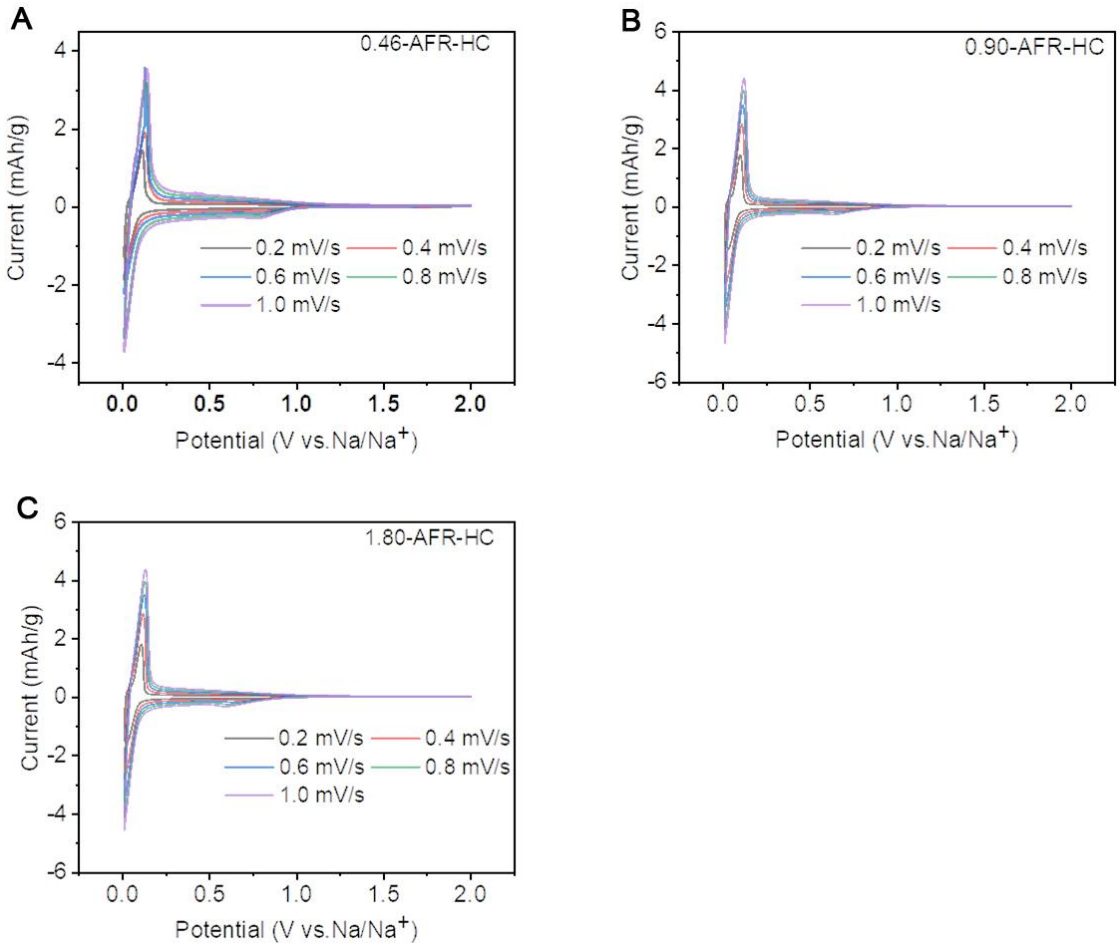

Supplementary Figure 14. CV curves at different scan rates of 0.2-1.0 $mV \cdot s^{-1}$. (A) 0.46-AFR-HC; (B) 0.90-AFR-HC; (C) 1.80-AFR-HC.

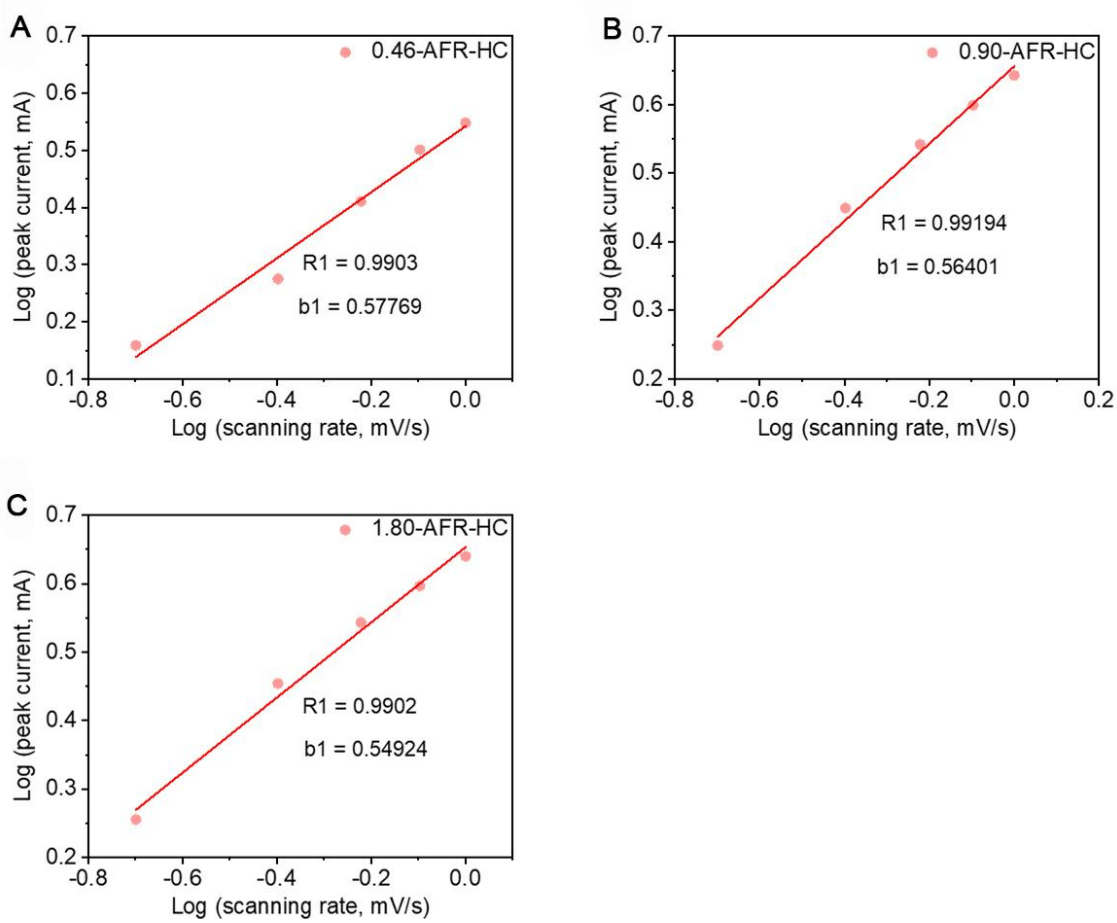

Supplementary Figure 15. Fitting results of b value for (A) 0.46-AFR-HC; (B) 0.90-AFR-HC; and (C) 1.80-AFR-HC electrodes.

REFERENCES

1. Wen Y, He K, Zhu Y, et al. Expanded graphite as superior anode for sodium-ion batteries. *Nat Commun* 2014;5:4033. [DOI: 10.1038/ncomms5033]

2. Yin X, Lu Z, Wang J, et al. Enabling Fast Na^+ transfer kinetics in the whole-voltage-region of hard-carbon anodes for ultrahigh-rate sodium storage. *Adv Mater* 2022;34:2109282. [DOI: 10.1002/adma.202109282]

3. Lu Z, Wang J, Feng W, et al. Zinc Single-atom regulated hard carbons for high rate and low temperature sodium ion batteries. *Adv Mater* 2023;35:2211461. [DOI: 10.1002/adma.202211461]

4. Wu F, Zhang M, Bai Y, Wang X, Dong R, Wu C. Lotus seedpod-derived hard carbon with hierarchical porous structure as stable anode for sodium-ion batteries. *ACS Appl Mater Interfaces* 2019:11:12554. [DOI: 10.1021/acsami.9b01419]

5. Hao M, Xiao N, Wang Y, et al. Pitch-derived N-doped porous carbon nanosheets with expanded interlayer distance as high-performance sodium-ion battery anodes. *Fuel Process Technol* 2018;177:328. [DOI: 10.1016/j.fuproc.2018.05.007]

6. Sun F, Wang H, Qu Z, et al. Carboxyl-dominant oxygen rich carbon for improved sodium ion storage: synergistic enhancement of adsorption and intercalation mechanisms. *Adv Energy Mater* 2020;11:2002981. [DOI: 10.1002/aenm.202002981]

7. Dong R, Zheng L, Bai Y, et al. Elucidating the mechanism of fast Na storage kinetics in ether electrolytes for hard carbon anodes. *Adv Mater* 2021;33:2008810. [DOI: 10.1002/adma.202008810]

8. Ma M, Cai H, Xu C, et al. Engineering solid electrolyte interface at nano-scale for high-performance hard carbon in sodium-ion batteries. *Adv Funct Mater* 2021;31:2100278. [DOI: 10.1002/adfm.202100278]

9. Yin X, Zhao Y, Wang X, et al. Modulating the graphitic domains of hard carbons derived from mixed pitch and resin to achieve high rate and stable sodium storage. *Small* 2022;18:2105568. [DOI: 10.1002/smll.202105568]

10. Li Y, Kong M, Hu J, Zhou J. Carbon-microcuboid-supported phosphorus-coordinated single atomic copper with ultrahigh content and its abnormal modification to Na storage behaviors. *Adv Energy Mater* 2020;10:2000400. [DOI: 10.1002/aenm.202000400]